ION DESOLVATION AS A MECHANISM FOR KINETIC ISOTOPE FRACTIONATION IN AQUEOUS SYSTEMS

Amy E. Hofmann[a,1]

Ian C. Bourg[a]

Donald J. DePaolo[a,b]

[a]Geochemistry Department, Earth Sciences Division, Lawrence Berkeley National Laboratory, Berkeley, CA 94720, USA.

[b]Department of Earth & Planetary Science, University of California, Berkeley, CA 94720, USA.

[1]To whom correspondence should be addressed:

Dr. Amy E. Hofmann
Center for Isotope Geochemistry
Lawrence Berkeley National Laboratory
1 Cyclotron Road Mail Stop 953-0473
Berkeley, CA 94720
aehofmann@lbl.gov
+1.717.201.7002

CLASSIFICATION: Physical Sciences—Earth, Atmospheric, & Planetary Sciences

Abstract

Molecular dynamics (MD) simulations show that the desolvation rates of isotopes of Li^+, K^+, Rb^+, Ca^{2+}, Sr^{2+}, and Ba^{2+} may have a relatively strong dependence on the metal cation mass. This inference is based on the observation that the exchange rate constant, k_{wex}, for water molecules in the first hydration shell follows an inverse power-law mass dependence ($k_{wex} \propto m^{-\gamma}$), where the coefficient γ is 0.05 ± 0.01 on average for all cations studied. Simulated water exchange rates increase with temperature and decrease with increasing isotopic mass for each element. The magnitude of the water exchange rate is different for simulations run using different water models (i.e., extended simple point charge (SPC/E) v. four-site transferrable intermolecular potential (TIP4P)); however, the value of the mass exponent γ is the same. Reaction rate theory calculations predict mass exponents consistent with those determined via MD simulations. The simulation-derived mass-dependences imply that solids precipitating from aqueous solution under kinetically controlled conditions should be enriched in the light isotopes of the metal cations relative to the solutions—consistent with measured isotopic signatures in natural materials and laboratory experiments. Desolvation effects are large enough that they may be a primary determinant of the observed isotopic fractionation during precipitation.

KEYWORDS: aqueous geochemistry, kinetic isotope effect, ligand exchange

Non-equilibrium processes are generally recognized as important influences on isotopic fractionation during mineral precipitation, especially at temperatures below a few hundred degrees C (1,2). Recent work in "non-traditional" stable isotopes (Li, Mg, Ca, Fe, Cd, Cu, etc.) has confirmed this inference and shown that non-equilibrium fractionation must be accounted for to understand global biogeochemical cycles involving these elements (2-5). A key observation is that light isotopes are preferentially incorporated into precipitating solids (6-8)—the opposite direction of enrichment expected for equilibrium fractionation, which depends on bond energetics (9,10). The origin of this non-equilibrium light-isotope enrichment is a key unknown in the isotopic geochemistry of mineral growth.

Calcite grown from aqueous solutions provides an excellent illustration of light-isotope enrichment during precipitation. Synthetically precipitated and natural samples of calcite and aragonite are fractionated relative to aqueous Ca^{2+} such that $\delta^{44/40}Ca$ in calcite is lower by 0.5 to 2‰ (7,11). Equilibrium Ca isotope fractionation between $Ca^{2+}_{(aq)}$ and calcite has not been measured in the laboratory, but studies of deep-sea sedimentary pore fluids suggest that the equilibrium fractionation is negligible: $\varepsilon_{eq} \approx 0.0 \pm 0.1$‰ (12). Growth of calcite from seawater-like aqueous solutions is not likely to be diffusion-limited for Ca, so the isotopic effects are inferred to be due to kinetic effects occurring at the solid-fluid interface (11,13). Diffusion in liquid water can result in kinetic isotopic fractionation (14-17), but in the case of Ca isotopes the available data suggest that the largest possible light-isotope enrichment from diffusion-limited growth is about 0.4‰ in $\delta^{44/40}Ca$, which is too small to explain the observations (17).

The growth of crystals from solution requires that the constituent solute ions undergo three steps: diffusion of solvated ions to the crystal-liquid interface, adsorption onto the solid surface, and incorporation into the crystal lattice. The last two steps entail a progressive desolvation of the ions; therefore, these steps may be rate-limited by solute dehydration (18,19). In support of this inference, molecular dynamics (MD) simulations of barium sulfate growth suggest that the kinetics of Ba^{2+} attachment—which govern barite nucleation and growth (20)—may be rate-limited by the partial desolvation of the metal to form an inner-sphere surface complex (21). Likewise, experimental (22,23), theoretical (13,24), and molecular simulation studies (25) suggest that the kinetics of metal

attachment at calcite surfaces may be related to the dehydration frequency of the metal near the surface. More broadly, the rate constants of several metal ligand-exchange reactions [Mg and Ni binding to a range of organic ligands (26,27), the dissolution of orthosilicate minerals containing a range of divalent metals (28,29)] have been shown to correlate with the water exchange rates of metals in liquid water, k_{wex} (the inverse of the residence time of water in the first solvation shell of the metal).

The correlation between metal-water exchange frequencies (k_{wex}) and the rates of other metal-ligand exchange reactions suggests—regardless of whether this correlation arises from desolvation being a rate-limiting step or from inherent similarities between different ligand-exchange reactions involving the same metal ion—that the isotopic mass dependence of k_{wex} may yield important insight into kinetic isotope fractionation during mineral growth and, more broadly, during metal biogeochemical cycling in aqueous systems. A mass-dependence of k_{wex}, though never previously reported, is in fact quite plausible within the framework of reaction rate theory, where k_{wex} is the product of a transmission coefficient (κ) of unknown mass dependence and a transition state theory rate constant (k^{TST}):

$$k_{wex} = \kappa\, k^{TST} \qquad (1).$$

As explained in more detail in the section "Theoretical basis of the mass dependence of k_{wex}", if metal-water distance is selected as the reaction coordinate (the simplest and most widespread choice for this type of reaction), k^{TST} has an inverse square root dependence on metal-water reduced mass μ_i; therefore, k_{wex} must vary with isotopic mass unless the unknown mass dependence of κ exactly cancels the strong mass-dependence of k^{TST}.

Molecular dynamics (MD) simulations are routinely used to investigate the k_{wex} values of alkali and alkaline earth metals in liquid water (30-35) and these simulations readily allow for the determination of the mass dependence of k_{wex} (15,17). Here, we use MD simulations in conjunction with reaction rate theory calculations to determine the isotopic mass dependence of k_{wex} for several common cations at three different temperatures, and we show that this dependence could account for the observed Ca isotopic effects attending calcite growth from aqueous solution.

Results and Discussion

Isotopic mass dependence of metal desolvation rates. For each 8 ns segment of our 16 ns simulations, we calculated the time-correlation function $C_{\mathrm{desolv}}(t)$, the average number of molecules that remain continuously located in the first solvation shell during a time interval of duration t. Water exchange rates k_{wex} were obtained by applying a linear least-squares regression to the first 20 ps of the first-order decay expression

$$\ln(C_{\mathrm{desolv}}) = -k_{\mathrm{wex}}\, t + \ln A_0 \qquad (2).$$

Grossfield (36) found that fitting the first 10 ps of similar autocorrelation functions was sufficient to model the lifetime of water molecules in the first solvation shell surrounding monovalent ions. Exchange rates calculated using Eq. 2 were evaluated for mass dependence by constructing log-log plots of $k_{\mathrm{wex},i}$ vs. m_i (for which the subscript i indicates the isotope) at each of the three simulation temperatures for the alkali (Figs. 1a and S1a) and alkaline earth metals (Figs. 1b and S1b). Data were fit with a linear least-square regression weighted by ± 1 s.e. on each value of $k_{\mathrm{wex},i}$ of the form

$$\log_{10}(k_{\mathrm{wex},i}) = \log_{10}(B) - \gamma \log_{10}(m_i) \qquad (3)$$

without constraints on either B or γ. Values of $k_{\mathrm{wex},i}$ are compiled in Supporting Information Dataset S1; values of B and γ are reported in Dataset S2a. Although Eq. 3 cannot be valid for infinitely high masses, it provides an accurate mathematical description of the relation between solute mass and water exchange rate for the mass range of most elements of interest ($m_i \approx$ 3 to 100 Da). [Within the precision of our simulations, plots of $k_{\mathrm{wex},i}$ vs. cation mass and plots of $k_{\mathrm{wex},i}$ vs. ion-water reduced mass μ_i both yield statistically robust fits to the k_{wex} data using Eq. 3 (values of B and γ calculated using μ_i instead of m_{i} in Eq. 3 are reported as B' and γ' in Dataset S2b), but the coefficient of variation of γ is, on average, 8 % larger for regressions of $k_{\mathrm{wex},i}$ vs. ion-water reduced mass. We therefore discuss our results in terms of γ-values (i.e., as a function of cation mass). We note that our key findings would be almost identical if we used γ'-values except insofar as the average γ-values of the six metals studied here are all identical (as described below), whereas the average γ'-values show a significant dependence on the type of metal with no obvious trend.] Calculated γ-values are significantly greater than zero in most cases. Therefore, metal desolvation rates have a significant isotopic mass dependence that is well described with the inverse power-law relation

$$k_{\mathrm{wex},i} \propto m_i^{-\gamma} \qquad (4).$$

The parameter B is significantly influenced by temperature, the type of metal, and the choice of water model (Dataset S2a). The temperature-dependence of B is consistent with an Arrhenius relation [$B \propto e^{-Ea/RT}$, where E_a (kJ mol^{-1}) is the phenomenological "activation energy" of B]. Our results yield an average E_a = 13.7 ± 2.6 kJ mol^{-1} (confidence intervals are reported as twice the standard error of the mean) for all solutes and water models investigated here, in agreement with the conceptual view of metal desolvation as a thermally activated process. The solute-dependence of B is consistent with X-ray diffraction data that show that solvating waters become more strongly oriented and more tightly bound to the central ion as surface charge density increases (30,36-38). This relationship translates into lower values of the radial distribution function, $g(r)$, of each cation at the boundary between the first and second solvation shell (Fig. S2; further details in SI Text and Table S1) and lower values of B and k_{wex} for smaller, higher-valence metals. The calculated values of k_{wex} depend more strongly on the nature of the solute than on the solvent as noted by (39); nevertheless, they are significantly influenced by the choice of water model (an indication, as pointed out by (40), of the difficulty in accurately predicting water exchange rates in molecular simulations). The value of the ratio $B_{TIP4P}/B_{SPC/E}$ is larger than one for four of the solutes studied here ($B_{TIP4P}/B_{SPC/E}$ = 1.45 ± 0.03, 1.11 ± 0.04, 2.20 ± 0.94, 1.58 ± 0.05 for Li^+, K^+, Sr^{2+}, Ba^{2+}, respectively; average values calculated from data at 278, 298 and 323 K), equal to one for one solute ($B_{TIP4P}/B_{SPC/E}$ = 1.02 ± 0.06 for Rb^+), and smaller than one for one solute ($B_{TIP4P}/B_{SPC/E}$ = 0.66 ± 0.10 for Ca^{2+}). We hypothesize that this water-model-dependence of B may result from a combination of dynamical and structural effects. Dynamically, water exchange rates and solute diffusion coefficients may be positively coupled (33), causing the four-site transferrable intermolecular potential (TIP4P) water model, which predicts faster self-diffusion of liquid water, to predict higher B values than the SPC/E model. Structurally, small differences in coordination may influence the lability of the solvation shell. For example, in the case of Ca^{2+}, the TIP4P water model yields an eight-fold coordination that may be particularly stable (Table S1).

In contrast to the sensitivity of B to temperature, water model, and type of metal, γ-values calculated with Eq. 3 show no significant dependence on these factors. Therefore, despite the water-model-dependent differences in the absolute values of $k_{wex,i}$, the mass-

dependence of k_{wex} is much less sensitive to simulation methodology. Ratios of γ-values calculated at different temperatures show that gamma is independent of T [$\gamma_{298K}/\gamma_{278K}$ = 0.83 ± 0.23 and $\gamma_{323K}/\gamma_{278K}$ = 1.26 ± 0.40; average values calculated for all water models and all solutes except Ba^{2+}, for which Eq. 3 yielded a negative γ-value at 278 K (the largest errors on gamma should occur where k_{wex} values are smallest, i.e., for divalent metals at 278 K)]. Ratios of gamma values obtained with different water models show that γ has little or no dependence on the choice of water model [$\gamma_{TIP4P}/\gamma_{SPC/E}$ = 0.64 ± 0.26, 1.09 ± 0.36, 0.93 ± 0.23, 1.49 ± 1.05, 0.32 ± 0.36, 0.41 ± 4.03 for Li^+, K^+, Rb^+, Ca^{2+}, Sr^{2+}, and Ba^{2+}, respectively, with an average value for all solutes and all temperatures (excepting Ba^{2+} at 278 K) of $\gamma_{TIP4P}/\gamma_{SPC/E}$ = 1.07 ± 0.37]. Averaging all gamma values obtained for the same solute, we obtain: γ_{Li} = 0.057 ± 0.015, γ_K = 0.049 ± 0.008, γ_{Rb} = 0.051 ± 0.007, γ_{Ca} = 0.043 ± 0.015, γ_{Sr} = 0.064 ± 0.035, γ_{Ba} = 0.032 ± 0.021. Our conclusion is that gamma is independent of the type of metal cation within the precision of our simulation methodology. Furthermore γ = 0.049 ± 0.009 adequately captures the results for all metals, temperatures, and water models investigated here, despite a range of k_{wex} values of over two orders of magnitude.

Theoretical basis of the mass dependence of k_{wex}. Transition state theory is widely used to explain the rates of metal desolvation and similar phenomena such as ion pair dissociation (31,35,41,42). Here, recalling that the rate constant for dissociation of a metal-water complex can be written as the product of κ and k^{TST} (Eq. 1), we show that this theory is consistent with our finding that k_{wex} decreases with metal isotopic mass, and also consistent with the magnitude of the mass dependence that comes from the MD simulations. Our object being to test whether reaction rate theory can predict a mass dependence of k_{wex}, we select the simplest and most widely used reaction coordinate (metal-water distance r) for evaluating κ and k^{TST} (31,33,41) [more conceptually complex choices of reaction coordinate are equally sound and may provide additional insights into k_{wex} (35,42)]. For each isotope (i) within this parameterization, k^{TST} depends only on the metal-water reduced mass μ_i and the centrifugally averaged effective potential $W_{eff,i}(r)$ {defined as $W_{eff,i}(r) = W_i(r) - 2\beta^{-1} \ln(r/r^{\ddagger})$, where $W_i(r) = -\beta^{-1} \ln[g_i(r)]$, $\beta = (k_B T)^{-1}$, k_B is Boltzmann's constant, and $r^{\ddagger}$ is the position of the top of the transition state barrier}:

$$k^{TST} = \sqrt{\frac{1}{2\pi\beta\mu_i}} \frac{e^{-\beta W_{\mathrm{eff},i}\left(r^{\ddagger}\right)}}{\int_0^{r^{\ddagger}} e^{-\beta W_{\mathrm{eff},i}(r)} dr} \qquad (5).$$

The transmission coefficient κ accounts for dynamical effects that are not included in k^{TST}, such as solvent reorganization kinetics during the dissociation of the metal-water pair (43-45). Here, we predict κ for each metal isotope using Kramers' model (46-48)

$$\kappa = \left[\left(\frac{\zeta_i}{2\mu_i\omega_i}\right)^2 + 1\right]^{1/2} - \frac{\zeta_i}{2\mu_i\omega_i} \qquad (6)$$

in which the reaction is modeled as a diffusive process characterized by a barrier frequency ω_i and a static friction coefficient ζ_i. The isotope-specific barrier frequency, ω_i, for each 8 ns simulation was calculated by fitting $W_{\mathrm{eff},i}(r)$ [derived as indicated above from $g_i(r)$] between $r^{\ddagger}$ ± 0.5 Å with the nonlinear inverse parabolic expression $W_{\mathrm{eff},i}(r) = W_{\mathrm{eff},i}(r^{\ddagger}) - \frac{1}{2}\mu_i\omega_i^2(r - r^{\ddagger})^2$ (30,47). The static friction coefficient was calculated with the implicit approximation that solute diffusion in water and solute-water dissociation have similar friction coefficients, and by applying the Stokes-Einstein relation $\zeta_i = k_{\mathrm{B}}T/D_i$ to the self-diffusion coefficient D_i of the solute in water. The latter was obtained from its velocity autocorrelation function via the Green-Kubo relation as described by (49) and following the procedure of (15) for 8 ns simulations. Alternative models of κ have been proposed that account for the frequency-dependence of ζ (47) as well as the anharmonicity of the reaction barrier and the dependence of ζ on reaction coordinate (50). For Na^+ desolvation in ambient liquid water, these more complex models predict κ values 1.7 to 5 times larger than obtained with Eq. 6, in line with MD simulation results (31). Below, we show that Kramers' model (Eq. 6) is sufficient to explain the mass dependence of k_{wex}, although it may underestimate κ by a factor of ~3.

The k_{wex} values predicted using reaction rate theory (Eqs. 1,5,6), hereafter named $k_{\mathrm{wex\_RR}}$, are plotted in Figs. 2 and S3 and compiled in SI Dataset S3. The regression lines plotted in Figs. 2 and S3 (black and dashed red for SPC/E and TIP4P, respectively) are weighted linear least squares fits to the $k_{\mathrm{wex\_RR}}$ data using Eq. 3. Errors on individual $k_{\mathrm{wex\_RR},i}$ values were determined solely from errors on κ_i, which were determined using a Monte Carlo routine to propagate errors on ζ_i and ω_i. The standard error on D_i during each 8 ns simulation (used to calculate the standard error on ζ_i) was calculated as $\sigma(D_i) = \sigma(D_{i,b})/\sqrt{n_b}$ in which $D_{i,b}$ is the block-averaged diffusion coefficient and n_b is the number of blocks. Each

8 ns simulation was divided into twenty 0.4 ns blocks to generate the statistical uncertainties. Predicted k_{wex_RR} values (Figs. 2 and S3) display the same general trends as those obtained by MD simulation (Figs. 1 and S1): k_{wex_RR} increases with temperature, decreases with the charge density of the metal, and is sensitive to the choice of water model. Water-exchange rates predicted with Eqs. 1,5,6 are consistently ~0.5 log units lower than those obtained by MD simulation, in agreement with the observation by (31) that Kramers' model underestimates κ by a factor of ~3 in the case of Na^+. The linear regressions in Figs. 2 and S3 are consistent with an inverse power-law mass dependence of k_{wex_RR} (Eq. 4) with slopes similar to those obtained by MD simulation. Thus, reaction rate theory calculations broadly support our MD simulation findings. The gamma values obtained from the linear regressions in Figs. 2 and S3 may be influenced by the approximations made in Eq. 6, but their average value ($\gamma = 0.038 \pm 0.021$) is close to our MD simulation result ($\gamma = 0.049 \pm 0.009$). The larger error on the RRT gamma is due to Ba calculations having an average gamma value of -0.001 ± 0.014. Ignoring Ba in both the MD and RRT determinations results in average γ values of 0.053 ± 0.007 and 0.046 ± 0.017, respectively.

Reaction rate theory also provides key insights into the fundamental basis of the observed mass dependence of desolvation frequency. In Fig. 3, we plot the contributions of k^{TST} and κ to our data on $\log k_{wex\_RR,i}$ v. $\log m_i$ for the representative case of Li^+ in SPC/E water at 298 K. The rate constant k^{TST} has an inverse square-root dependence on ion-water reduced mass, as expected from Eq. 5. Hence, if κ had no isotopic mass-dependence, one would expect a strong, inverse square-root dependence of k_{wex_RR} on the reduced mass μ_i. Simulations by Møller et al. (33) suggest that such a strong mass dependence of k_{wex} exists for Li^+ in supercritical water, where κ should be close to unity. Our calculations using Eq. 6, however, predict that κ has a positive mass-dependence in liquid water that attenuates the overall inverse-mass dependence of k_{wex_RR}.

Conceptually, the transmission coefficient κ describes the fraction of trajectories—among all trajectories where a metal-water complex reaches the transition state—where the metal-water complex returns to its original state without dissociating (so-called barrier recrossings). A direct interpretation of our results is that the chance of barrier recrossing decreases as solute mass increases. Additional insight can be gained by noting that κ also

describes the influence of solvent dynamics (the collective dynamics of all molecules except those directly involved in the metal-water dissociation reaction) on the reaction rate (41) [k^{TST} is influenced by solvent structure through $W(r)$ in Eq. 5, but it is independent of solvent dynamics]. Our results show that solvent dynamics have a decreasing influence on k_{wex} as solute mass increases, perhaps because the slower motions of heavy solutes allow more time for solvent reorganization to accommodate the dissociation of the metal-water complex.

On the broader topic of kinetic isotope effects, our results yield two important insights. First, the inverse mass-dependence of k_{wex} (Eq. 4) may provide a clue into the fundamental basis of the isotopic mass dependence of solute diffusion coefficients in liquid water [$D_i \propto m_i^{-\beta}$ (14-17)], because solute D values are positively correlated with k_{wex} at least in the case of Li^+ and Na^+ in liquid water (33). Second, our simulations, in which isotopes have identical interatomic interaction parameters and differ only by their masses, show that—in addition to the expected quantum mechanical effects—classical mechanical effects can play an important role in causing kinetic isotope fractionations in geochemical systems, as pointed out by Young et al. (51). This finding is consistent with studies showing that Newtonian mechanics are the primary cause of carbon kinetic isotope effects associated with the dimerization of cyclopentadiene (52) and may contribute significantly to a range of oxygen kinetic isotope effects (53).

Implications for isotopic fractionation in geochemical processes. Our finding of the isotopic mass dependence of k_{wex} implies that any ligand-exchange reaction whose rate constant correlates with k_{wex} [mineral dissolution (28,29), metal binding to organic ligands (26,27), and possibly metal attachment to mineral surfaces (13,18,19,21)] should exhibit significant kinetic isotope fractionation. For such reactions, the overall kinetic isotope fractionation ($\alpha_{kinetic}$) has a maximum value in conditions where the forward reaction rate is much larger than the backward rate. This maximum value can be readily determined from the ratio of water desolvation rates of two different isotopes (i and j) of a given metal ion:

$$\alpha_{kinetic} = \frac{k_{wex,i}}{k_{wex,j}} = \left(\frac{m_i}{m_j}\right)^{-\gamma} \qquad (7).$$

In cases where the backward rate is non-negligible, calculation of $\alpha_{kinetic}$ is straightforward but requires knowledge of the ratio of forward to backward reaction rates (13). In cases for which these rates are not well constrained, the maximum value of $\alpha_{kinetic}$ calculated via Eq. 7 may be used to deduce the ratio of forward to backward rates from the measured overall kinetic isotope fractionation.

Using the global MD-derived gamma value (γ = 0.049 ± 0.009) and the isotopic masses given in Dataset S1, we can calculate the maximum value of $\alpha_{kinetic}$ for the metals studied here. Results (Table 1) show that the mass-dependence of k_{wex} can account for relatively large kinetic isotope fractionations equal to or greater than the magnitude of observed light-isotopic enrichments in solids containing Li (8), Ca (7), and Ba (6). It should be noted that each of these three studies (6-8) documents mineral precipitation from aqueous solutions with ionic concentrations greater than infinite dilution (as considered here) and containing other ligands in addition to water. Although the magnitude and direction of the measured fractionations in (6-8) coincide with those predicted by our simulations, the extent to which our results are directly transferable to these multicomponent systems—or to systems in which metal desolvation is extremely rapid relative to crystal growth rate or the metal is bound to a surface, an oligomer, or to an anion as a solvated contact ion pair—is unclear and should be the focus of further studies.

In the case of inorganic calcite precipitation, a recent study by Nielsen et al. (24) shows that Ca isotopic signatures in calcite reflect contributions from kinetic processes, which become more important at higher growth rates. The kinetic contribution is expected to be important (13,24) because the characteristic time-scale of Ca attachment to calcite kink sites—on the order of microseconds (24,54)—is faster than the characteristic time-scale of Ca detachment by a factor of 2 to >20 at typical supersaturation values used in laboratory experiments. Calcite growth rates and Ca isotope fractionations are consistent with a ratio of $^{44}Ca^{2+}$ to $^{40}Ca^{2+}$ binding rate constants (k_{44Ca}/k_{40Ca}) of order 0.9920 to 0.9963 (24). Our molecular-scale value of $\alpha_{kinetic}$ = 0.9953 ± 0.0009 ($^{44/40}$Ca, Table 1) for a single step desolvation is similar in magnitude to the observed effects associated with calcite growth. This may be a coincidence, but our interpretation is that our simulations show that isotope effects associated with a key step in the crystal growth process (54) are of the

correct sign and magnitude to explain the observed experimental results and hence are a potential source of the kinetic fractionation associated with crystal growth.

Because we calculated the desolvation rates of only a subset of alkali and alkaline earth metal cations, there is no *a priori* expectation that our results should apply to other solutes, or even to other metals. Nevertheless, the few available data on kinetic isotope effects associated with ligand exchange reactions of aquated metals other than those studied here are remarkably consistent with Eq. 7 and our predicted mass-dependence of k_{wex}. For example, Eq. 7 with $\gamma = 0.049 \pm 0.009$ predicts $\alpha_{kinetic}(^{114/110}Cd) = 0.9982$ and $\alpha_{kinetic}(^{65/63}Cu) = 0.9985$, in agreement with the kinetic isotope fractionations measured during cadmium uptake by freshwater phytoplankton [$\alpha_f(^{114/110}Cd) = 0.9986 \pm 0.0006$ (55)] and during copper binding to azurin enzyme, a kinetically-controlled one-step process [$\alpha_f(^{65/63}Cu) = 0.99847$ (56)].

Simulation Methods

Molecular dynamics simulations involving one cation and 550 water molecules in a periodically replicated, cubic simulation cell were performed using the program MOLDY 3.6 (57). Each simulation was carried out for 16 ns (with a 1 fs time step) in the NVE ensemble and was preceded by 202 ps of equilibration at the desired temperature. Due to the absence of a counter-ion and the application of periodic boundary conditions, these simulations approximate conditions of infinite dilution (15-17,30-35). We chose to model all alkali and alkaline earth metal cations that have more than one naturally occurring stable isotope (Li^+, K^+, Rb^+, Ca^{2+}, Sr^{2+}, Ba^{2+}) with the exception of Mg^{2+}, for which preliminary calculations showed too few water-exchange events to accurately calculate k_{wex} via direct simulation. Each metal cation was simulated at three different temperatures (278, 298, and 323 K) and for a range of solute isotopic masses (both naturally occurring and hypothetical) from m = 3 to 176 Da (Dataset S1). Simulation cell volume was fixed to the corresponding liquid water densities at 1 atm (ρ = 1.000, 0.997, and 0.988 g cm^{-3}, respectively). Ion-water interaction potentials (Table S2) were taken from (58). To determine the sensitivity of simulation results to the choice of water model, we replicated each simulation with two widely used water models: the extended simple point charge

(SPC/E) model (59) and the four-site transferrable intermolecular potential (TIP4P) model (60). A comparison of the models' predictions for the physical properties of liquid water is given in the SI Text.

Long-range interactions are treated by Ewald summation in three dimensions with a real space cutoff at r_c = 9.63 Å, a reciprocal space cutoff at k_c = 1.91 Å^{-1}, and a sensitivity/screening factor of α = 0.3151 Å^{-1}, resulting in an Ewald sum accuracy of > 99.9%. Molecular trajectories are calculated using a modified form of the Beeman algorithm [the most accurate of all "Verlet-equivalent" algorithms (57)] to solve the Newton-Euler equations of motion. We divided each simulation into two 8 ns blocks for data analysis. The total energy varied by less than 1% during each 8 ns simulation, indicating excellent energy conservation and justifying our decision to not couple the simulation box to an external thermostat (15,17).

Unlike Impey et al. (30) and others (31-32,35) who allowed water molecules to make temporary (i.e., ≤2 ps) excursions from the hydration sphere and still be counted as present within the sphere, in our calculations of the time-correlation function $C_{\mathrm{desolv}}(t)$ we do not count water molecules as being present in the first hydration sphere once they move beyond a distance of r_{min} from the cation. [We tested the "2-ps-excursion" method of (30) and found that it yields lower k_{wex} values (as expected), but the same mass dependence of k_{wex} in almost all cases. The exception was Ca^{2+}, the metal with the lowest water-exchange rates of all the solutes in this study, for which we hypothesize that the k_{wex} values calculated with the 2-ps-excursion method may have been too small to accurately probe their mass dependence.] The desolvation correlation functions for all monovalent cations are qualitatively the same (i.e., e-folding times of ca. 10-50 ps), regardless of temperature or water model; likewise, the desolvation correlation functions calculated for divalent cations all have e-folding times of ca. 200-600 ps.

ACKNOWLEDGMENTS

Support for this work was provided by the Center for Isotope Geochemistry, funded by the U.S. Department of Energy, Director, Office of Science, Office of Basic Energy Sciences

under Contract No. DE-AC02-05CH11231, as well as through the Center for Nanoscale Control of Geologic CO_2, an Energy Frontier Research Center.

References

1. Cole DR, Ohmoto H (1986) Kinetics of isotope exchange at elevated temperatures and pressures. *Stable Isotopes in High Temperature Geological Processes. Reviews in Mineralogy*, eds JW Valley, HP Taylor Jr, and JR O'Neil (Mineralogical Society of America, Washington, DC) Vol 16, pp 41–90.

2. Johnson CM, Beard BL, Albarède F (2004) *Geochemistry of Non-Traditional Stable Isotopes*. *Reviews in Mineralogy and Geochemistry*, Vol 55 (Mineralogical Society of America and Geochemical Society, Washington, DC).

3. Stumm W, Morgan JJ (1996) *Aquatic chemistry: Chemical equilibria and rates in natural waters*. (Wiley, New York).

4. Anbar AD, Rouxel O (2007) Metal stable isotopes in paleoceanography. *Annu. Rev. Earth Planet. Sci*. 35: 717–746.

5. Baskaran M (2011) *Handbook of Environmental Isotope Geochemistry* (Springer-Verlag, Berlin).

6. Böttcher ME, et al (2011) Barium isotope fractionation during formation of anhydrous barium carbonate (witherite): Influence of experimental conditions. *Geophysical Research Abstracts* 13: EGU2011-4982-1.

7. Nielsen LC, Druhan JL, Yang W, Brown ST, DePaolo DJ (2011) Calcium isotopes as tracers of biogeochemical processes. *Handbook of Environmental Isotope Geochemistry,* ed M Baskaran (Springer-Verlag, Berlin), Vol 1, pp 105-124.

8. Wunder B, Meixner A, Romer RL, Jahn S (2011) Li-isotope fractionation between silicates and fluids: Pressure dependence and influence of the bonding environment. *Eur. J. Mineral.* 23: 333–342.

9. Bigeleisen J, Mayer MG (1947) Calculation of equilibrium constants for isotopic exchange reactions. *J. Chem. Phys.* 15: 261–267.

10. Bigeleisen J (1965) Chemistry of isotopes. *Science* 147: 463–471.

11. DePaolo DJ (2004) Calcium isotope variations produced by biological, kinetic, radiogenic, and nucleosynthetic processes. *Geochemistry of Non-Traditional Stable Isotopes. Reviews in Mineralogy and Geochemistry,* eds CM Johnson, BL Beard, and F Albarède (Mineralogical Society of America and Geochemical Society, Washington, DC) Vol 55, pp 255–288.

12. Fantle MS, DePaolo DJ (2007) Ca isotopes in carbonate sediment and pore fluid from ODP Site 807A: The Ca^{2+}(aq)-calcite equilibrium fractionation factor and calcite

recrystallization rates in Pleistocene sediments. *Geochim. Cosmochim. Acta* 71: 2524–2546.

13. DePaolo DJ (2011) Surface kinetic model for isotopic and trace element fractionation during precipitation of calcite from aqueous solutions. *Geochim. Cosmochim. Acta* 75: 1039–1056.

14. Richter FM, et al (2006) Kinetic isotope fractionation during diffusion of ionic species in water. *Geochim. Cosmochim. Acta* 70: 277–289.

15. Bourg IC, Sposito G (2007) Molecular dynamics simulations of kinetic isotope fractionation during the diffusion of ionic species in liquid water. *Geochim Cosmochim. Acta* 71: 5583–5589.

16. Bourg IC, Sposito G (2008) Isotopic fractionation of noble gases by diffusion in liquid water: Molecular dynamics simulations and hydrologic applications. *Geochim. Cosmochim. Acta* 7: 2237–2247.

17. Bourg IC, Richter FM, Christensen JN, Sposito G (2010) Isotopic mass dependence of metal cation diffusion coefficients in liquid water. *Geochim. Cosmochim. Acta* 74: 2249–2256.

18. Nielsen AE (1984) Electrolyte crystal growth mechanisms. *J. Cryst. Growth* 67: 289–310.

19. Nielsen AE, Toft JM (1984) Electrolyte crystal growth kinetics. *J. Cryst. Growth* 67: 278–288.

20. Kowacz M, Putnis C, Putnis A (2007) The effect of cation:anion ratio in solution on the mechanism of barite growth at constant supersaturation: Role of the desolvation process on the growth kinetics. *Geochim. Cosmochim. Acta* 71: 5168–5179.

21. Piana S, Jones F, Gale JD (2006) Assisted desolvation as a key kinetic step for crystal growth. *J. Am. Chem. Soc.* 128: 13568–13574.

22. deBoer RB. (1977) Influence of seed crystals on the precipitation of calcite and aragonite. *Am. J. Sci.* 277: 38–60.

23. Mucci A, Morse JW (1983) The incorporation of Mg^{2+} and Sr^{2+} into calcite overgrowths: Influences of growth rate and solution composition. *Geochim. Cosmochim. Acta* 47: 217–233.

24. Nielsen LC, DePaolo DJ, De Yoreo JJ (2012) Self-consistent ion-by-ion growth model for kinetic isotopic fractionation during calcite precipitation. *Geochim. Cosmochim. Acta* 86: 166–181.

25. Kerisit S, Parker SC (2004) Free energy of adsorption of water and metal ions on the {10-14} calcite surface. *J. Am. Chem. Soc.* 126: 10152–10161.

26. Casey WH, Ludwig C (1995) Silicate mineral dissolution as a ligand-exchange reaction. *Chemical Weathering Rates of Silicate Minerals. Reviews in Mineralogy*, eds AF White and SL Brantley (Mineralogical Society of America, Washington, DC) Vol 31, pp 87–117.

27. Richens DT (2005) Ligand substitution reactions at inorganic centers. *Chem. Rev.* 105: 1961–2002.

28. Casey WH (1991) On the relative dissolution rates of some oxide and orthosilicate minerals. *J. Colloid Interf. Sci.* 146: 586–589.

29. Casey WH, Westrich HR (1992) Control of dissolution rates of orthosilicate minerals by divalent metal-oxygen bonds. *Nature* 355: 157–159.

30. Impey RW, Madden PA, McDonald IR (1983) Hydration and mobility of ions in solution. *J. Phys. Chem.* 87: 5071–5083.

31. Rey R, Hynes JT (1996) Hydration shell exchange kinetics: An MD study for Na^+(aq). *J. Phys. Chem.* 100: 5611–5615.

32. Koneshan S, Rasaiah JC, Lynden-Bell RM, Lee SH (1998) Solvent structure, dynamics, and ion mobility in aqueous solutions at 25°C. *J. Phys. Chem. B* 102: 4193–4204.

33. Møller KB, Rey R, Masia M, Hynes JT (2005) On the coupling between molecular diffusion and solvation shell exchange. *J. Chem. Phys.* 122: 114508.

34. Rustad JR, Stack AG (2006) Molecular dynamics calculation of the activation volume for water exchange on Li^+. *J. Am. Chem. Soc.* 128: 14778–14779.

35. Kerisit S, Rosso KM (2009) Transition path sampling of water exchange rates and mechanisms around aqueous ions. *J. Chem. Phys.* 131: 114512.

36. Grossfield A (2005) Dependence of ion hydration on the sign of the ion's charge. *J. Chem. Phys.* 122: 024506.

37. Ohtaki H, Radnai T (1993) Structure and dynamics of hydrated ions. *Chem. Rev.* 93: 1157–1204.

38. Collins KD, Neilson GW, Enderby JE (2007) Ions in water: Characterizing the forces that control chemical processes and biological structure. *Biophys. Chem.* 128: 95–104.

39. Dunand FA, Helm L, Merbach AE (2003) Solvent exchange on metal ions. *Adv. Inorg. Chem.* 54: 1–69.

40. Wang J, Rustad JR, Casey WH (2007) Calculation of water-exchange rates on aqueous polynuclear clusters and at oxide-water interfaces. *Inorg. Chem.* 46: 2962–2964.

41. Masia M, Rey R (2003) Reaction rate theory approach to thermodynamic state dependence of hydration shell exchange for Li^{+}(aq) *J. Phys. Chem. B* 107: 2651–2659.

42. Truhlar DG, Garrett BC (2000) Multidimensional Transition State Theory and the Validity of Grote-Hynes Theory. *J. Phys. Chem. B* 104: 1069–1072.

43. Eyring H (1935a) The activated complex in chemical reactions. *J. Chem. Phys.* 3: 107–115.

44. Eyring H. (1935b) The activated complex and the absolute rate of chemical reactions. *Chem. Rev.* 17: 65–77.

45. Wigner E (1938) The Transition State Method. *Trans. Faraday Soc.* 34: 29–41.

46. Kramers HA (1940) Brownian motion in a field of force and the diffusion model of chemical reactions. *Physica* 7: 284–304.

47. Grote RF, Hynes JT (1980) The stable states picture of chemical reactions. II. Rate constants for condensed and gas phase reaction models. *J. Chem. Phys.* 73: 2715–2732.

48. Ciccotti G, Ferrario M, Hynes JT, Kapral R (1990) Dynamics of ion pair interconversion in a polar solvent. *J. Chem. Phys.* 93: 7137–7147.

49. Frenkel D, Smit B (2002) *Understanding Molecular Simulation: From Algorithms to Applications, 2nd Ed.* (Academic Press, San Diego).

50. Voth GA (1992) A theory for treating spatially-dependent friction in classical activated rate processes. *J. Chem. Phys.* 97: 5908–5910.

51. Young ED, Galy A, Nagahara H (2002) Kinetic and equilibrium mass-dependent isotope fractionation laws in nature and their geochemical and cosmochemical significance. *Geochim. Cosmochim. Acta* 66: 1095–1104.

52. Kelly KK, Hirschi JS, Singleton DA (2009) Newtonian kinetic isotope effects. Observation, prediction, and origin of heavy-atom dynamic isotope effects. *J. Am. Chem. Soc.* 131: 8382–8383.

53. Roth JP (2009) Oxygen isotope effects as probes of electron transfer mechanisms and structures of activated O_2. *Accounts Chem. Res.* 42: 399–408.

54. Stack A, Raiteri P, Gale JD (2012) Accurate rates of the complex mechanisms for growth and dissolution of minerals using a combination of rare-event theories. *J. Am. Chem. Soc.* 134: 11–14.

55. Lacan F, Francois R, Youngcheng J, Sherrell RM (2006) Cadmium isotopic composition in the ocean. *Geochim. Cosmochim. Acta* 70: 5104–5118.

56. Zhu XK, et al (2002) Mass fractionation processes of transition metal isotopes. *Earth Planet. Sci. Lett.* 200: 47–62.

57. Refson K (2000) Moldy: a portable molecular dynamics simulation program for serial and parallel computers. *Comput. Phys. Commun.* 126: 310–329.

58. Åqvist J (1990) Ion-water interaction potentials derived from free energy perturbation simulations. *J. Phys. Chem.* 94: 8021–8024.

59. Berendsen HJC, Grigera JR, Straatsma TP (1987) The missing term in effective pair potentials. *J. Phys. Chem.* 91: 6269–6271.

60. Jorgensen WL, Chandrasekhar J, Madura JD, Impey RW, Klein ML (1983) Comparison of simple potential functions for simulating liquid water. *J. Chem. Phys.* 79: 926–935.

Figures and Figure Captions

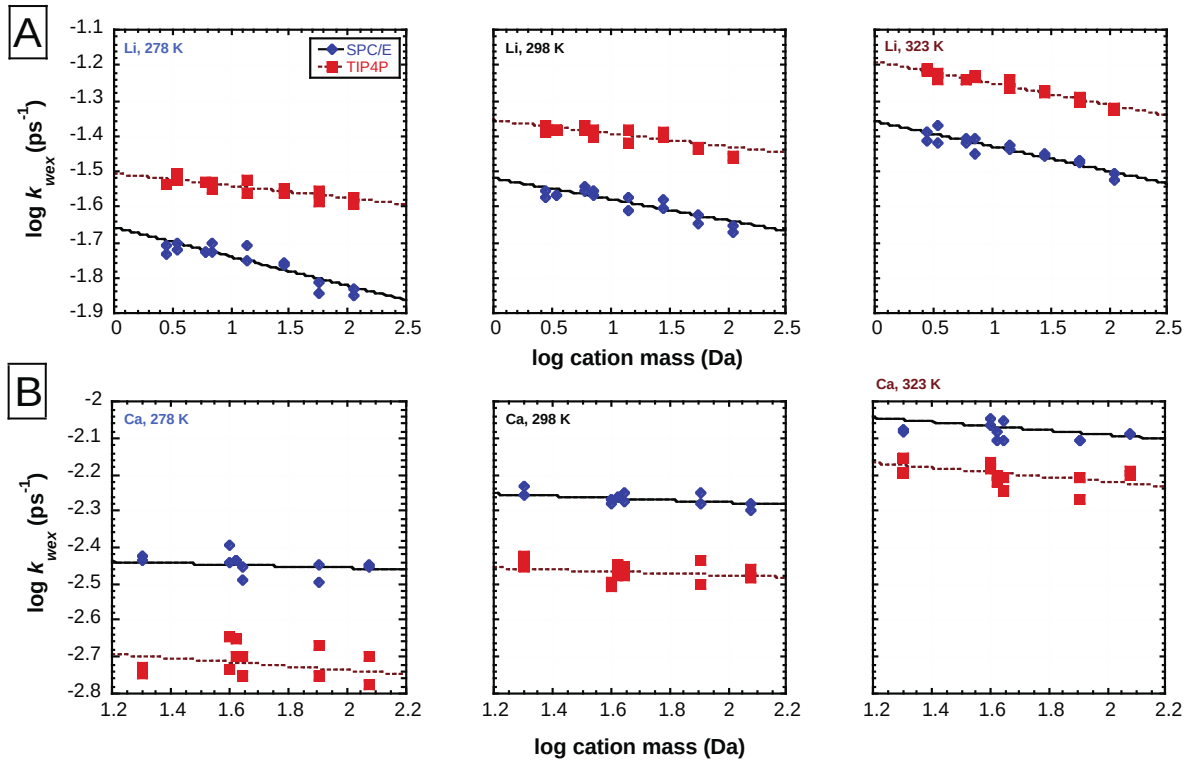

Figure 1. Log-log plots of water exchange rates (k_{wex}) determined via MD simulation vs. cation isotopic mass for a range of isotopes (given in Dataset S1) of (A) Li^+ and (B) Ca^{2+}. Each row presents results at three different temperatures, increasing from left to right. Results obtained with the SPC/E and TIP4P water models are plotted as blue diamonds and red squares, respectively. Regression lines are weighted linear least squares fits to the data using Eq. 3. Error bars (in most cases smaller than symbol size) are one standard error of the regression from Eq. 2. Similar results were obtained for K^+, Rb^+, Sr^{2+}, and Ba^{2+} isotopes as shown in Figure S1.

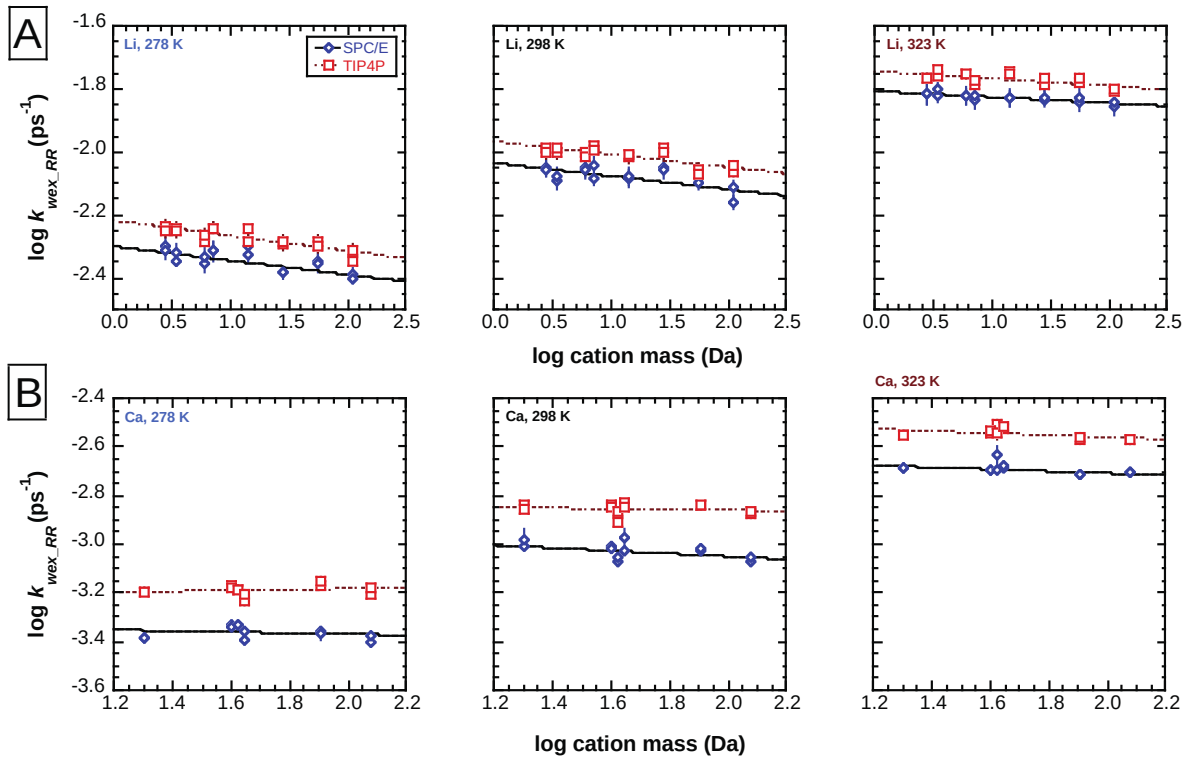

Figure 2. Same as Figure 1 for water exchange rates ($k_{\mathrm{wex\_RR}}$) determined via reaction rate theory (using values of ζ_i and ω_i from MD simulations) vs. cation isotopic mass. Error bars on the symbols are one standard error determined via a Monte Carlo propagation of errors on ω_i and ζ_i as detailed in the text. Similar results were obtained for K^+, Rb^+, Sr^{2+}, and Ba^{2+} isotopes as shown in Figure S3.

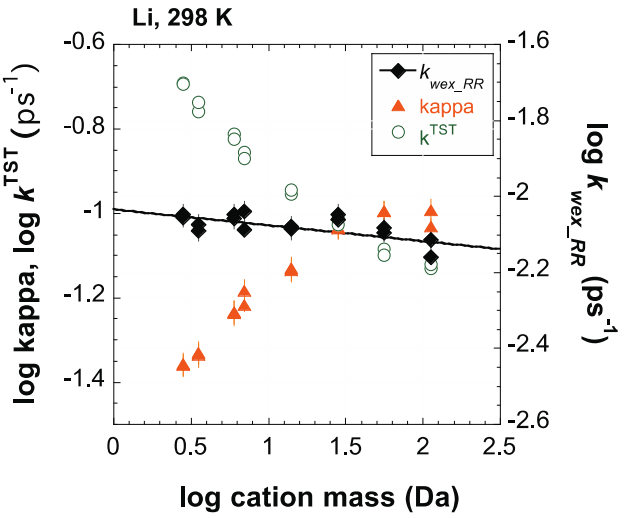

Figure 3. Analysis of the contributions of k^{TST} and κ to the mass dependence of k_{wex_RR} (shown for Li^+ isotopes in SPC/E water at 298 K). Values of k^{TST} (open green circles, left vertical axis) for each isotope of Li^+ were calculated using Eq. 5; values of κ (orange triangles, left vertical axis) were determined using Eq. 6. Each k_{wex_RR} value (black diamonds, right vertical axis) is the product of κ and k^{TST}. The regression line is a weighted linear least squares fit to the data using Eq. 3.

Tables

Table 1. Predicted isotopic fractionations based on MD simulation results

Isotopic System	$\alpha_{dynamic}$	‰ (solid)
$^{7}Li/^{6}Li$	0.9925 ± 0.0014	-7.5 ± 1.4
$^{41}K/^{39}K$	0.9976 ± 0.0004	-2.4 ± 0.4
$^{87}Rb/^{85}Rb$	0.9989 ± 0.0002	-1.1 ± 0.2
$^{44}Ca/^{40}Ca$	0.9953 ± 0.0009	-4.7 ± 0.9
$^{88}Sr/^{86}Sr$	0.9989 ± 0.0002	-1.1 ± 0.2
$^{137}Ba/^{134}Ba$	0.9989 ± 0.0002	-1.1 ± 0.2

Fractionations are reported as both alpha values and solid phase isotopic signatures and were calculated using the MD global γ = 0.049 ± 0.009 and the dynamic fractionation factor defined in Eq. 7. Errors are two standard error.

Supporting Information

Cation-water structure calculations and comparison to experimental data. Solute-water radial distribution functions g(r), also known as pair correlation or pair distribution functions, were calculated with a subroutine of the Moldy program using center-of-mass coordinates. Radial distribution functions—as derived from 8 ns 298 K SPC/E simulations—for the major isotope of each ion are plotted for illustrative purposes in Fig. S2a (monovalent ions) and S2b (divalent ions). The insets in Figure S2 show the approximate location of each RDF global minimum (r_{min}), interpreted as the radial extent of the first solvation shell (1). We calculated the average coordination number N_{w} of each isotopic species via the summation

$$N_w = \sum_0^{r_{min}} g(r) 4\pi r^2 \Delta r \qquad \text{(S1)}$$

for each 8 ns simulation. In Table S1, we give coordination numbers for each cation, averaged over all isotopic species, for the total 16 ns simulation time. It should be noted that predicted and measured coordination numbers are sensitive to the value of r_{min} if $g(r_{\mathrm{min}})$ is much greater than zero; therefore, the errors cited for a given cation in Table S1 are the larger of either: two standard deviation of N_w values for all isotopic species or the amount by which the average N_w would change if r_{min} were varied by ± 0.1 Å. The range in experimentally determined coordination numbers given in Table S1 is due in part to analytical differences in the actual distances probed (e.g., between nuclei versus between centers of electron clouds, which may be polarized) and to the concentration of ions in solution, with larger coordination numbers measured in systems with lower ion concentrations (2). Our simulations are all at "infinite dilution" and, as expected, generally produce coordination numbers at the higher end of the range of experimentally determined values. It is important to note that our calculated coordination numbers are non-integer averages; the fractional nature of these values is due to the fact that the coordination number reported in many studies is the most probable but not necessarily the only thermodynamically stable value: some fraction of the solvated ion population will have lower and higher coordination numbers due to only slight differences in the free energies of those complexes (3). In the case of Rb^+, the coordination number given for comparison to our simulation-derived N_{w} values is from MD simulations by (4) rather than

from experiments; the lack of X-ray diffraction data for Rb^+ is due to the fact that Rb^+ fluoresces upon irradiation at the most commonly used wavelengths (2). Experimentally determined coordination numbers and those calculated from MD simulations for all cations modeled in this study generally agree (Table S1), which we take as evidence in support of our simulation methodology.

Comparison of SPC/E and TIP4P water models to experimentally determined properties of water. Both water models accurately predict the density (5,6) and O-O radial distribution functions of ambient liquid water (7); however, the structure of hydrogen bonding in the two models differs significantly (8), and these differences may affect each model's ability to reproduce certain physical properties of water. In particular, the two models differ in the accuracy of their predictions of the self-diffusion of water and its static dielectric constant. The self-diffusion coefficient of SPC/E water at 298 K (obtained from one of our Li^+ MD simulations) is $\sim 2.4 \times 10^{-9}$ m^2 s^{-1}, which falls within ~5% of the published experimental value [2.3×10^{-9} m^2 s^{-1} (9)]; however, the self-diffusion coefficient of TIP4P water at 298 K ($\sim 3.3 \times 10^{-9}$ m^2 s^{-1}) overestimates the experimentally determined self-diffusivity by ~45%. In terms of the dielectric constant of liquid water, SPC/E predicts a value within ~10% of the actual value at 298 K (10), whereas the TIP4P value is within ~40% at 293 K, improving to within ~30% at 373 K (11). In short, the TIP4P model predicts weaker hydrogen bonding and faster dynamics than the SPC/E model.

SI Text References

1. Impey RW, Madden PA, McDonald IR (1983) Hydration and mobility of ions in solution. *J. Phys. Chem.* 87: 5071–5083.

2. Ohtaki H, Radnai T (1993) Structure and dynamics of hydrated ions. *Chem. Rev.* 93: 1157–1204.

3. Ikeda T, Boero M, Terakura K (2007) Hydration properties of magnesium and calcium ions from constrained first principles molecular dynamics. *J. Chem. Phys.* 127:074503.

4. Koneshan S, Rasaiah JC, Lynden-Bell RM, Lee SH (1998) Solvent structure, dynamics, and ion mobility in aqueous solutions at 25°C. *J. Phy. Chem. B* 102: 4193–4204.

5. Berendsen HJC, Grigera JR, Straatsma TP (1987) The missing term in effective pair potentials. *J. Phys. Chem.* 91: 6269–6271.

6. Jorgensen WL, Chandrasekhar J, Madura JD, Impey RW, Klein ML (1983) Comparison of simple potential functions for simulating liquid water. *J. Chem. Phys.* 79: 926–935.

7. Sorenson JM, Hura G, Glaeser RM, Head-Gordon T (2000) What can x-ray scattering tell us about the radial distribution functions of water? *J. Chem. Phys.* 113: 9149–9161.

8. Peltz C, Baranyai A, Chialvo AA, Cummings PT (2003) Microstructure of water at the level of three-particle correlation functions as predicted by classical intermolecular models. *Molecular Simulation* 29: 13–21.

9. Mills R (1973) Self-diffusion in normal and heavy water in the range 1–45°C. *J. Phys. Chem.* 77: 685–688.

10. Kusalik PG, Svishchev IM (1994) The spatial structure in liquid water. *Science* 265: 1219–1221.

11. Neumann M (1986) Dielectric relaxation in water. Computer simulations with the TIP4P potential. *J. Chem. Phys.* 85: 1567–1580.

SI Figures and Figure Legends

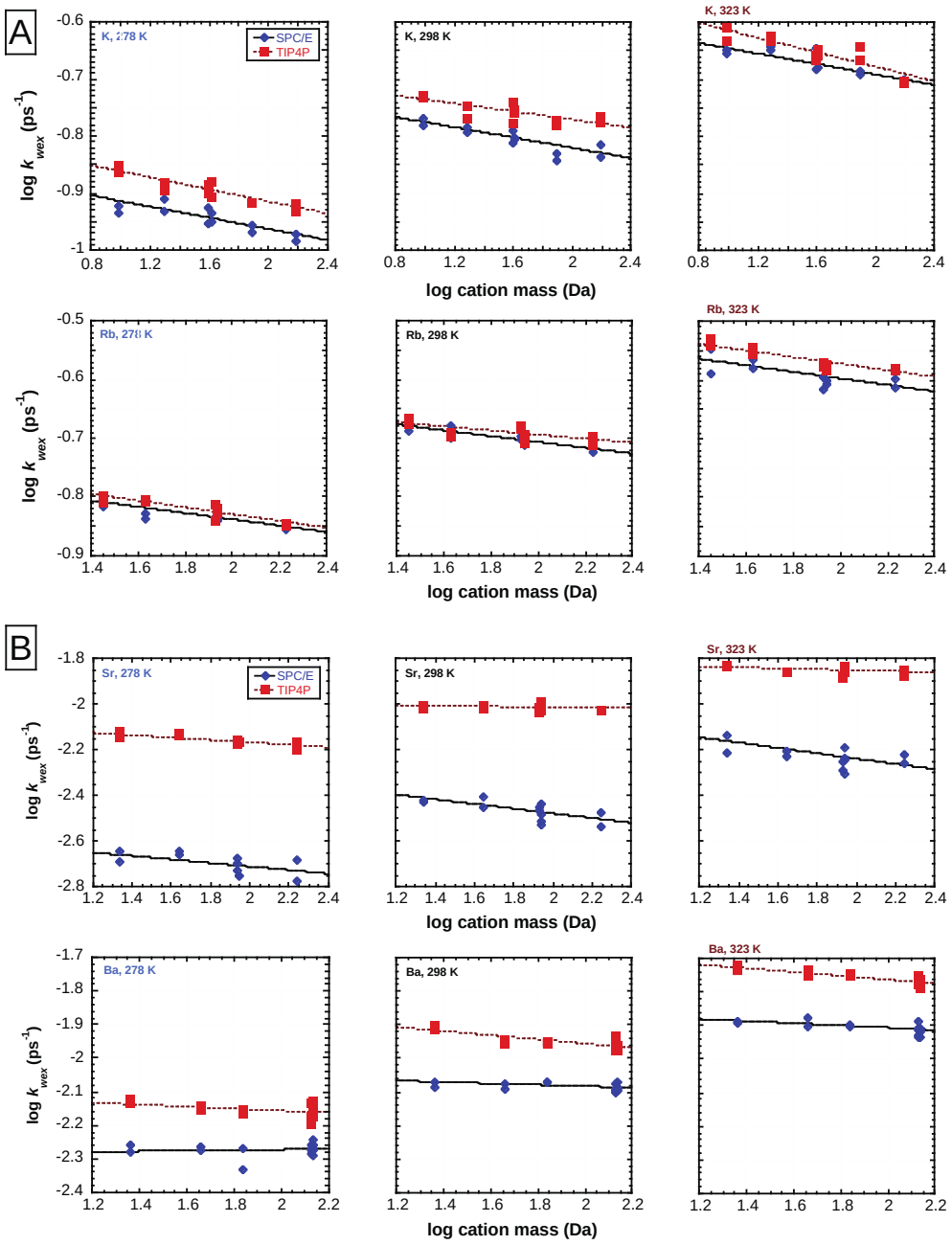

Figure S1. Log-log plots of water exchange rates (k_{wex}) determined via MD simulations vs. cation isotopic mass for isotopes given in Dataset S1 of (A) monovalent (K^+, Rb^+) and (B) divalent (Sr^{2+}, Ba^{2+}) cations. Each row presents results at three different temperatures, increasing from left to right. Results obtained with the SPC/E and TIP4P water models are plotted as blue diamonds and red squares, respectively. Regression lines are weighted linear least squares fits to the data using Eq. 2. Error bars (in most cases smaller than symbol size) are one standard error of the regression from Eq. 1.

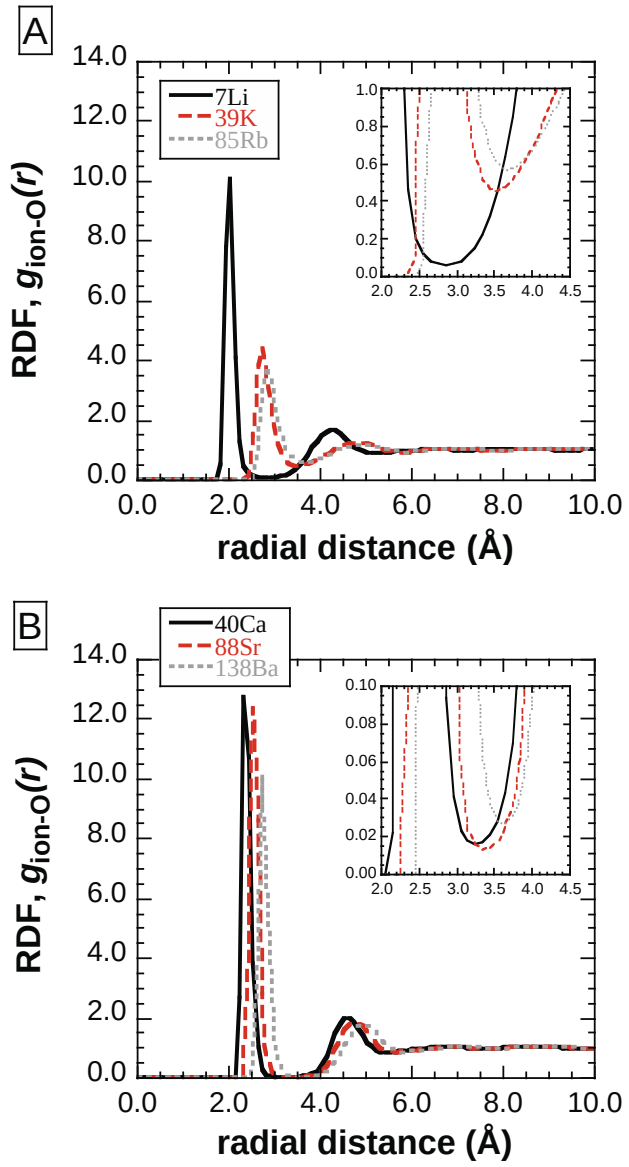

Figure S2. Ion-water radial distribution functions (RDFs) from 8 ns MD simulations of (a) monovalent and (b) divalent ions in SPC/E water at 298 K. Inset shows the approximate location of each RDF global minimum, which is interpreted as the radial extent of each ion's first solvation shell. Note that the scale on the y-axis of the inset in panel b is an order of magnitude smaller than that of the inset in panel a.

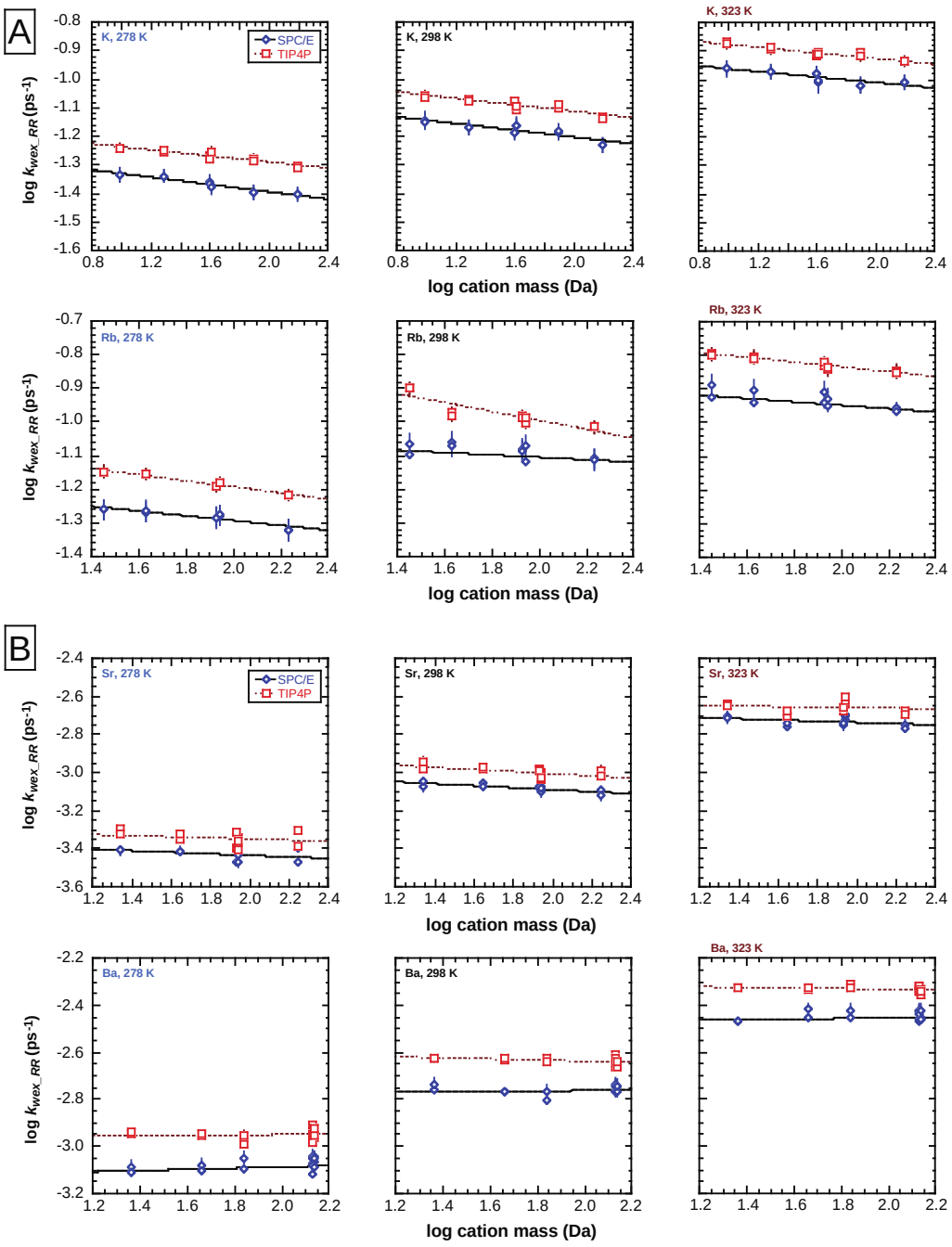

Figure S3. Same as Figure S1 for water exchange rates (k_{wex_RR}) determined via reaction rate theory (using values of D_i and ω_i from MD simulations) vs. cation isotopic mass. Error bars on the symbols are one standard error determined via a Monte Carlo propagation of errors on ω_i and ζ_i as detailed in the text.

Table S1. Cation coordination numbers from MD simulations.

Solute	Average Cation Coordination Number (# H_2O, ± 2σ†)						Experimental Coordination Numbers
	278 K		298 K		323 K		
	SPC/E	TIP4P	SPC/E	TIP4P	SPC/E	TIP4P	
Li^+	4.37 ± 0.04	5.34 ± 0.04	4.39 ± 0.04	5.30 ± 0.04	4.41 ± 0.04	5.24 ± 0.04	~3-6[2], 4–6[3,5]
K^+	6.66 ± 0.24	6.83 ± 0.20	6.68 ± 0.24	6.91 ± 0.24	6.68 ± 0.24	7.08 ± 0.30	3-6,8[2], 5.5[3], 5.5-6.4[4], 4-8[5], 6.1[6]
Rb^+	7.02 ± 0.32	7.38 ± 0.28	7.16 ± 0.36	7.45 ± 0.30	7.27 ± 0.34	7.45 ± 0.30	7.9[1*]
Ca^{2+}	7.71 ± 0.08	7.99 ± 0.02	7.68 ± 0.06	7.98 ± 0.02	7.63 ± 0.04	7.97 ± 0.02	5.5-7,10[2], 6–10[3], 6.8[7]
Sr^{2+}	8.06 ± 0.02	8.66 ± 0.04	8.08 ± 0.02	8.65 ± 0.02	8.09 ± 0.02	8.63 ± 0.04	7.9,8[2], 6–8,10[3], 6.8[6], 7.8[8]
Ba^{2+}	8.83 ± 0.02	9.12 ± 0.02	8.83 ± 0.02	9.14 ± 0.02	8.81 ± 0.04	9.15 ± 0.04	9.5[2]

Coordination numbers were calculated for each 8 ns simulation using Eq. S1; these values were then averaged. Experimentally determined coordination numbers are given for comparison.

†Coordination numbers are sensitive to the value of $r_{\min}$ if $g_{iO}(r_{\min})$ is much greater than zero; therefore, the errors cited for a given cation are the larger of either: two standard deviation of N_w values for all isotopic species (alkaline earth metals) or the amount by which the average N_w would change if r_{min} were varied by ± 0.1 Å (alkali metals).
*Note that this is an MD result: Ohtaki and Radnai (2) attest that Rb^+ is not probed with X-rays due to fluorescence.

Table S1 References

1. Koneshan S, Rasaiah JC, Lynden-Bell RM, Lee SH (1998) Solvent structure, dynamics, and ion mobility in aqueous solutions at 25°C. *J. Phy. Chem. B* 102: 4193–4204.

2. Ohtaki H, Radnai T (1993) Structure and dynamics of hydrated ions. *Chem. Rev.* 93: 1157–1204.

3. Obst S, Bradaczek H (1996) Molecular dynamics study of the structure and dynamics of the hydration shell of alkaline and alkaline-earth metal cations. *J. Phys. Chem.* 100: 15677–15687.

4. Soper AK, Wickstrom K (2006) Ion solvation and water structure in potassium halide aqueous solutions. *Biophys. Chem.* 124: 180–191.

5. Varma S, Rempre SB (2006) Coordination numbers of alkali metal ions in aqueous solutions. *Biophys. Chem.* 124: 192–199.

6. Dang LX, Schenter GK, Glezakou V-A, Fulton JL (2006) Molecular simulation analysis and X-ray absorption measurement of Ca^{2+}, K^{+}, and Cl^{-} ions in solution. *J. Phys. Chem. B* 110: 23644–23654.

7. Fulton JL, Heald SM, Badyal YS, Simonson JM (2003) Understanding the effects of concentration on the solvation of Ca^{2+} in aqueous solution. I: The perspective on local structure from EXAFS and XANES. *J. Phys. Chem. A* 107: 4688–4696.

8. Seward TM, Henderson CMB, Charnok JM, Dreisner T (1999) An EXAFS study of solvation and ion pairing in aqueous strontium solutions to 300°C *Geochim. Cosmochim. Acta* 63, 2409–2418.

Table S2. Lennard-Jones 6–12 potential function parameters used to describe short-range interactions between cations *i* and water (oxygen) *O* in MD simulations.

Atom	SPC/E[1]			TIP4P		
	σ_{io} (Å)	ε_{io} (kJ/mol)	*q (e)*	σ_{io} (Å)	ε_{io} (kJ/mol)	*q (e)*
H	-	-	+0.4238	-	-	+0.52
O	3.16556	0.65017	-0.8476	3.15365	0.64852	0[2]
Li	2.59447	0.89205	+1	2.58958	0.89083	+1
K	3.95228	0.11942	+1	3.94484	0.11927	+1
Rb	4.21849	0.05924	+1	4.21055	0.08604	+1
Ca	2.76320	4.42395	+2	2.75799	4.41833	+2
Sr	3.13393	2.26843	+2	3.12803	2.26555	+2
Ba	3.47587	1.43174	+2	3.46929	1.42992	+2

The terms $2^{1/6}\sigma_{ij}$ and ε_{ij} equal the location and depth of the LJ potential minimum, respectively. Cation-oxygen interaction parameters were calculated following Lorentz-Berthelot combining rules.

[1]It should be noted that the Åqvist (1) interaction potentials given here were calculated for the SPC water model, which was not used in this study. SPC and SPC/E water models differ only by a small difference in their partial atomic charges.
[2]TIP4P utilizes a 4-site model of the water molecule in which the negative charge is reduced to -1.04 *e* at a single point, M, which is located at the bisection of the H—O—H angle and 0.15 Å from the O atom.

Table S2 Reference

1. Åqvist J (1990) Ion-water interaction potentials derived from free energy perturbation simulations. *J. Phys. Chem.* 94: 8021–8024.